Resolving near-field from high order signals of scattering near-field scanning optical microscopy

Nan Zhou, Yan Li, and Xianfan Xu*

School of Mechanical Engineering and Birck Nanotechnology Center, Purdue University, West Lafayette, Indiana 47907, USA

*xxu@purdue.edu

Abstract: The ability of using scattering-type near-field scanning optical microscopy (s-NSOM) to characterize amplitude and phase of optical near fields was investigated. We employ numerical simulations to compute signals scattered by the tip, using a bowtie nano-aperture as the example, and compare with the data obtained from s-NSOM measurements. Through demodulation of higher order harmonic signals, we show that, with the increasing order of harmonic signals, both the simulated and measured near fields are in closer agreement with the anticipated near field results. The polarization-resolved detection also helps to establish a tip-dependent transfer matrix that relates the local field components with the s-NSOM signals, which characterizes the scattering of the tip with respect to different field components. This work illustrates the importance of using higher order signals in obtaining near field in an s-NSOM measurement.

OCIS codes: (180.4243) Near-field microscopy; (310.6628) Subwavelength structures, nanostructures.

References and links

1. F. Keilmann and R. Hillenbrand, "Near-field microscopy by elastic light scattering from a tip," Philos Trans A Math Phys Eng Sci **362**(1817), 787–805 (2004).
2. A. Bek, R. Vogelgesang, and K. Kern, "Apertureless scanning near field optical microscope with sub-10 nm resolution," Rev. Sci. Instrum. **77**(4), 043703 (2006).
3. L. Gomez, R. Bachelot, A. Bouhelier, G. P. Wiederrecht, S. Chang, S. K. Gray, F. Hua, S. Jeon, J. A. Rogers, M. E. Castro, S. Blaize, I. Stefanon, G. Lerondel, and P. Royer, "Apertureless scanning near-field optical microscopy: a comparison between homodyne and heterodyne approaches," J. Opt. Soc. Am. A **23**(5), 823–833 (2006).
4. R. Hillenbrand and F. Keilmann, "Complex optical constants on a subwavelength scale," Phys. Rev. Lett. **85**(14), 3029–3032 (2000).
5. N. Ocelic, A. Huber, and R. Hillenbrand, "Pseudoheterodyne detection for background-free near-field spectroscopy," Appl. Phys. Lett. **89**(10), 101124 (2006).
6. S. Aubert, A. Bruyant, S. Blaize, R. Bachelot, G. Lerondel, S. Hudlet, and P. Royer, "Analysis of the interferometric effect of the background light in apertureless scanning near-field optical microcopy," J. Opt. Soc. Am. B **20**(10), 2117 (2003).
7. A. J. Huber, F. Keilmann, J. Wittborn, J. Aizpurua, and R. Hillenbrand, "Terahertz Near-Field Nanoscopy of Mobile Carriers in Single Semiconductor Nanodevices," Nano Lett. **8**(11), 3766–3770 (2008).
8. F. Huth, M. Schnell, J. Wittborn, N. Ocelic, and R. Hillenbrand, "Infrared-spectroscopic nanoimaging with a thermal source," Nat. Mater. **10**(5), 352–356 (2011).
9. A. C. Jones and M. B. Raschke, "Thermal Infrared Near-Field Spectroscopy," Nano Lett. **12**(3), 1475–1481 (2012).
10. K. G. Lee, H. W. Kihm, J. E. Kihm, W. J. Choi, H. Kim, C. Ropers, D. J. Park, Y. C. Yoon, S. B. Choi, D. H. Woo, J. Kim, B. Lee, Q. H. Park, C. Lienau, and D. S. Kim, "Vector field microscopic imaging of light," Nat. Photonics **1**(1), 53–56 (2007).
11. M. Rang, A. C. Jones, F. Zhou, Z. Y. Li, B. J. Wiley, Y. Xia, and M. B. Raschke, "Optical near-field mapping of plasmonic nanoprisms," Nano Lett. **8**(10), 3357–3363 (2008).
12. R. L. Olmon, M. Rang, P. M. Krenz, B. A. Lail, L. V. Saraf, G. D. Boreman, and M. B. Raschke, "Determination of Electric-Field, Magnetic-Field, and Electric-Current Distributions of Infrared Optical Antennas: A Near-Field Optical Vector Network Analyzer," Phys. Rev. Lett. **105**(16), 167403 (2010).
13. T. G. Habteyes, S. Dhuey, K. I. Kiesow, and A. Vold, "Probe-sample optical interaction: size and wavelength dependence in localized plasmon near-field imaging," Opt. Express **21**(18), 21607–21617 (2013).
14. M. Schnell, A. Garcia-Etxarri, J. Alkorta, J. Aizpurua, and R. Hillenbrand, "Phase-Resolved Mapping of the Near-Field Vector and Polarization State in Nanoscale Antenna Gaps," Nano Lett. **10**(9), 3524–3528 (2010).

#213948 - $15.00 USD Received 11 Jun 2014; revised 15 Jul 2014; accepted 18 Jul 2014; published 25 Jul 2014

15. B. Knoll and F. Keilmann, "Near-field probing of vibrational absorption for chemical microscopy," Nature **399**(6732), 134–137 (1999).
16. A. Cvitkovic, N. Ocelic, and R. Hillenbrand, "Analytical model for quantitative prediction of material contrasts in scattering-type near-field optical microscopy," Opt. Express **15**(14), 8550–8565 (2007).
17. S. Amarie and F. Keilmann, "Broadband-infrared assessment of phonon resonance in scattering-type near-field microscopy," Phys. Rev. B **83**(4), 045404 (2011).
18. A. García-Etxarri, I. Romero, F. J. Garcia de Abajo, R. Hillenbrand, and J. Aizpurua, "Influence of the tip in near-field imaging of nanoparticle plasmonic modes: Weak and strong coupling regimes," Phys. Rev. B **79**(12), 125439 (2009).
19. R. Esteban, R. Vogelgesang, and K. Kern, "Full simulations of the apertureless scanning near field optical microscopy signal: achievable resolution and contrast," Opt. Express **17**(4), 2518–2529 (2009).
20. R. Fikri, T. Grosges, and D. Barchiesi, "Apertureless scanning near-field optical microscopy: numerical modeling of the lock-in detection," Opt. Commun. **232**(1-6), 15–23 (2004).
21. S. Diziain, D. Barchiesi, T. Grosges, and P. M. Adam, "Recovering of the apertureless scanning near-field optical microscopy signal through a lock-in detection," Appl. Phys. B **84**(1-2), 233–238 (2006).
22. W. Chen, A. Kimel, A. Kirilyuk, and T. Rasing, "Apertureless SNOM study on gold nanoparticles: Experiments and simulations," Phys. Status Solidi B **247**(8), 2047–2050 (2010).
23. R. Esteban, R. Vogelgesang, and K. Kern, "Apertureless near-field optical microscopy: Differences between heterodyne interferometric and non-interferometric images," Ultramicroscopy **111**(9-10), 1469–1474 (2011).
24. A. Ravichandran, E. C. Kinzel, J. C. Ginn, J. A. D'Archangel, E. Z. Tucker, B. A. Lail, M. B. Raschke, and G. D. Boreman, "Numerical Modeling of Scattering Type Scanning Near-Field Optical Microscopy," Proc. SPIE **8815**, 88150S (2013).
25. E. D. Palik, *Handbook of Optical Constants of Solids* (Academic, 1998).
26. P. B. Johnson and R. W. Christy, "Optical constants of the noble metals," Phys. Rev. B **6**(12), 4370–4379 (1972).
27. R. L. Olmon, P. M. Krenz, A. C. Jones, G. D. Boreman, and M. B. Raschke, "Near-field imaging of optical antenna modes in the mid-infrared," Opt. Express **16**(25), 20295–20305 (2008).
28. E. X. Jin and X. Xu, "Plasmonic effects in near-field optical transmission enhancement through a single bowtie-shaped aperture," Appl. Phys. B **84**(1-2), 3–9 (2006).
29. R. Esteban, R. Vogelgesang, and K. Kern, "Tip-substrate interaction in optical near-field microscopy," Phys. Rev. B **75**(19), 195410 (2007).
30. A. Bouhelier, M. R. Beversluis, and L. Novotny, "Near-field scattering of longitudinal fields," Appl. Phys. Lett. **82**(25), 4596–4598 (2003).
31. K. G. Lee, H. W. Kihm, K. J. Ahn, J. S. Ahn, Y. D. Suh, C. Lienau, and D. S. Kim, "Vector field mapping of local polarization using gold nanoparticle functionalized tips: independence of the tip shape," Opt. Express **15**(23), 14993–15001 (2007).
32. Y. Li, N. Zhou, E. C. Kinzel, X. Ren, and X. Xu, "The origin of interferometric effect involving surface plasmon polariton in scattering near-field scanning optical microscopy," Opt. Express **22**(3), 2965–2972 (2014).

1. Introduction

Scattering type NSOM (s-NSOM) is an optical technology for achieving super-resolution on the order of 10 nm, which is largely independent of wavelength [1, 2]. A sharp tip in the vicinity of the sample serves as a scatterer that converts evanescent near fields to propagating radiation, making near fields detectable by far field detectors. An important undertaking for s-NSOM is to suppress the large background signal, which is a result of the light scattering from the sample and the tip shaft [3]. This is achieved by modulating the near field interaction through sinusoidally oscillating the tip and collecting data using interferometric methods [4–6]. Taking advantage of the fact that the background signal usually has a slower spatial variation than that of useful near field signals, the near field information can be extracted by demodulating the total signal into higher harmonics of tip vibration. Interferometric techniques are incorporated to resolve both amplitude and phase of the near fields.

s-NSOM has found its application in a wide range of frequencies and with various sample types, for example, characterizing mobile carriers in semiconductors in THz frequencies [7], studying phonon modes in polar materials [8, 9], and mapping near field vectors/modes of optical plasmonic devices that offer subwavelength manipulation of light [10–14]. Because of the interaction between tip and near fields, and the complex configuration for background suppression, data collection and interferometry detection, s-NSOM images often show discrepancy compared with true optical near fields. Analytical models that approximate the probe tip as a point dipole [1, 15] or a finite-sized dipole [16, 17] provide fundamental understandings of the interaction between a tip and a flat surface, where an effective polarizability was derived considering the geometry and optical properties of both the sample

#213948 - $15.00 USD Received 11 Jun 2014; revised 15 Jul 2014; accepted 18 Jul 2014; published 25 Jul 2014

and tip materials. On the other hand, numerical computations are necessary to gain insights into the mechanism of near-field interaction and to understand the effect of various geometry and experimental parameters and to obtain the true near field information. This is also crucial for characterizing the tip, interpreting measurement results, and optimizing and calibrating the system.

Accurate interpretations of near field vectors produced by nanostructures require both amplitude and phase of all the near field components are recovered. In this work, we use the bowtie aperture as an example to demonstrate resolving the near field components in the visible frequency using higher order modes. 3D simulations incorporating a signal demodulation scheme are used to calculate the intensity and phase of different polarizations in the far field originating from the interaction of a long dielectric or metallic tip with the field produced by the bowtie aperture. The calculated scattered far fields agree with the s-NSOM data. Comparison between these calculated and measured far field data with the anticipated near field indicates the importance of demodulating signals at higher harmonics.

2. Modeling of s-NSOM signal

2D and 3D numerical simulations of s-NSOM measurements have been carried out [18–24]. Numerical simulations are generally capable of handling important components such as samples with complex patterns, the tip, the oscillation of the tip, and polarization dependent scattered intensity. In [19], full simulations of s-NSOM signals on a gold inclusion were carried out. A recent study [24] computed the interaction between the probe and a patch antenna in the infrared to map the vertical component of the near field.

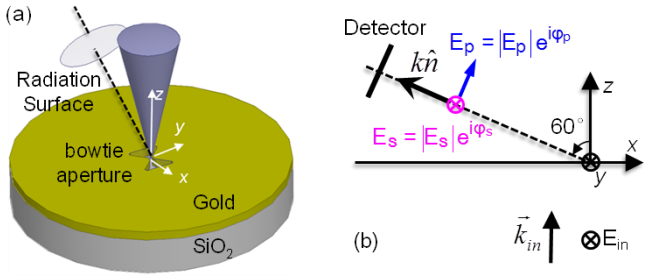

Fig. 1. (a) Simulation model of the tip, the bowtie aperture and the substrate. The scattering intensity is collected along the -*x* axis with an off-normal angle of 60 degree. (b) Illustration of the collection path and far field polarizations.

In this work, we use a finite-element method (FEM) solver (HFSS, Ansoft LLC) to compute s-NSOM signals. The model is similar as that in [24] and is given in Fig. 1(a). The tip is modeled as having a conical shape and a full angle of 25 degree. The radius of the tip at the apex is 10 nm for a Si tip and 30 nm for an Au coated Si tip, which are close to the apex radii of commercial tips used in measurements. A bowtie aperture made in gold film on SiO_2 substrate is used as sample. A *y*-polarized Gaussian beam at 633 nm wavelength with a 1 μm waist illuminates the bowtie aperture from the substrate side. Far field signals within a solid angle of 0.265 sr are collected by an objective lens (60° off-normal). In the calculation, the radiated fields are computed based on the integration of the field values over a radiation surface (see Fig. 1(a)) by applying the Green theorem. Optical properties of silicon and gold are taken from [25] and [26], respectively. Figure 1(b) shows the details of the collection orientation vector $\hat{n}$ and the far field polarization directions *s* and *p* associated with it. Under this configuration, E_s and E_p signals are related to the in-plane local field E_y and out-of-plane local field E_z, respectively. A 2D far field signal map can be produced by assembling E_s and E_p at each *x*, *y* location.

For many symmetric plasmonic nanostructures such as dipole antenna [12, 27] and bowtie aperture [14, 28], one of the near field components is negligible. Figure 2 shows the characteristic near field produced by a 200 nm bowtie aperture in a 100 nm thick gold film, with a gap of 20 nm. The incident *y*-polarized electric field drives charges to accumulate at

#213948 - $15.00 USD Received 11 Jun 2014; revised 15 Jul 2014; accepted 18 Jul 2014; published 25 Jul 2014

the gap edges, leading to one E_y spot inside the gap with constant phase and two E_z spots with a π-phase shift across the gap. The intensity of the E_x component is about one order of magnitude lower compared with the other two components. Experimentally the measured E_p signal is dominated by the E_z component (Fig. 1). The confinement in the y direction and the near field phase behavior can be represented by the field distribution along a characteristic line, indicated by the red dashed line in Fig. 2.

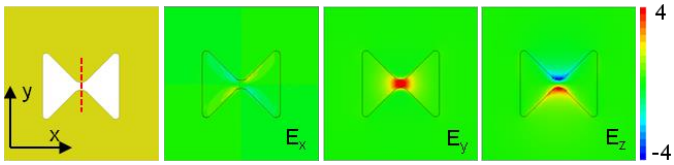

Fig. 2. Numerical simulations of the field distributions for local E_x, E_y and E_z in a 400 × 400 nm^2 region.

To investigate the effects of tip materials on the scattered signal, we first analyze the computed phases for *s* and *p* polarizations by comparing the results obtained using Si and Au tips. Figure 3 shows the phases along the characteristic line at several tip sample distances *z*, from 2 nm to 42 nm. The phase at the position y = 50 nm is the zero phase reference. From Figs. 3(a) and 3(b) we see that with a Si tip, φ_s is almost a constant across the gap and there is a 180 degree shift for φ_p at the gap center, except at very small tip sample distance φ_p is slightly off 180 degrees. These are in agreement with the phase behavior of the local fields without the presence of a tip, as shown in Fig. 2. Therefore, the dielectric tip does not distort near field phases. However, with a metallic tip, phase distortion is significant as shown in Figs. 3(c) and 3(d). Generally, metallic tips interact much stronger with the sample than dielectric tips and thus provide a large signal strength. On the other hand, the local plasmonic modes and spectral behavior under study could be distorted using metallic tips, which are dependent on the specific tip shape [29] and position [18]. Dielectric tips, in contrary, work in the weak coupling regime with minimum perturbation of near-field modes and spectral responses [18, 19]. In addition, metallic tips usually have a relatively large apex radius because of the coating. Therefore, in terms of interpreting experimental images without introducing phase distortion and obtaining a higher spatial resolution, a dielectric tip is preferred. For the rest of this work, we will focus on resolving near-fields by Si tip only.

Figure 4 shows the simulated far field amplitude of a bowtie aperture under the constant height scan mode, where the tip-sample distance *z* is fixed at 5 nm. There is one spot at the gap center for $|E_s|$, and two spots in the vicinity of apexes are mapped for $|E_p|$, in agreement with the local field shown in Fig. 2. However, the computed images, which contain both near field signal and background/tip scattering, show a slow spatial variation and thus a much larger spot size than that of the real local fields shown in Fig. 2. The constant tip-sample distance scan therefore does not accurately resolve the near field spot size. We show below that modeling of tip oscillation and high order demodulation is needed to resolve the near field.

#213948 - $15.00 USD Received 11 Jun 2014; revised 15 Jul 2014; accepted 18 Jul 2014; published 25 Jul 2014

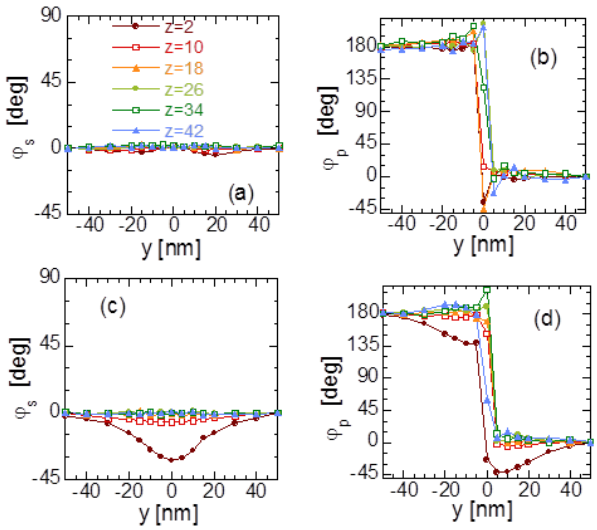

Fig. 3. Calculated phases in the far field with Si tip (top row) and Au coated Si tip (bottom row), at different tip-sample distance z. The legend is the same for all plots. y positions are from –50 nm to 50 nm.

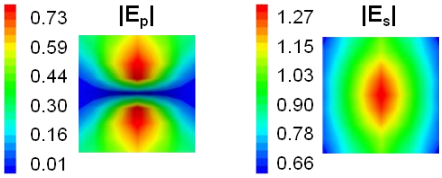

Fig. 4. Calculated amplitude $|E_s|$ and $|E_p|$, with a constant tip-sample separation of 5 nm. The images have a dimension of 100 × 100 nm^2. The tip moves with a step of 25nm for both *x* and *y* directions.

The modeling of vertical tip oscillation is illustrated in Fig. 5(a). Assuming a sinusoidal oscillation at a frequency Ω, the tip-sample separation is given by $z(t) = z_{avg} + A\cos(\Omega t)$, where z_{avg} is the average distance and A is the oscillation amplitude. We set z_{avg} and A as 17 nm and 16 nm, respectively, thus the minimum tip-sample distance is 1 nm. Because of the sinusoidal modulation of the near field interaction, the obtained signals are also sinusoidal. Let $S(z(t)) = S(t)$ denotes the time-dependent signal (either s- or p-polarization) when the tip is at a position (x, y), which is computed by integrating the far field signal over the detection solid angle. To model the demodulation signal at the n-th order harmonics, we calculate the Fourier transform at $n\Omega$ [4, 20] as:

$$E_n \propto \int_0^T S(t)e^{-in\Omega t}dt \propto \int_0^{T/2} S(t)\cos(n\Omega t)dt, \qquad (1)$$

where symmetry of the function has been applied.

Figures 5(b) and 5(c) show the signals as a function of tip height at different *y* positions, along the center dashed line in Fig. 2. It is clear that with an increasing distance between the tip and sample surface, $|E_p|$ decays rapidly as a result of the decrease of the vertical near field interaction strength, while $|E_s|$ signals in Fig. 5(b), corresponding to the amplitude of the in-plane component E_y, are not so sensitive to the tip-sample distance. To compute the integral Eq. (1) with these discrete data, two methods can be applied. As in [20], Eq. (1) was first re-written as an integral with respect to *z* and then discretized in the spatial domain. This requires a large number of simulations at different *z* positions to minimize the discretization

#213948 - $15.00 USD Received 11 Jun 2014; revised 15 Jul 2014; accepted 18 Jul 2014; published 25 Jul 2014

error. Here we first fitted the data to obtain continuous functions $|E_s(z)|$ (or $|E_s(t)|$) and $|E_p(z)|$ ($|E_p(t)|$) at each y position and then substituted these functions into Eq. (1). $|E_s(z)|$ was fitted using an exponential function $S(z) = a + b\exp(cz)$. $|E_p(z)|$ was fitted using a power function $S(z) = (a + bz^c)^{-1}$, motivated by the z^{-3} dependence in a point dipole model [15] and the z^{-2} dependence in the finite dipole model [16]. At y = 10 nm, the fitting parameters are a = 0.093, b = 0.030 and c = 1.021 for $|E_p(z)|$. Similarly, c is between 1 and 1.25 for curves corresponding to other y positions. This indicates that with a more realistic modeling of the tip shape, the decay of the near field interaction becomes slower.

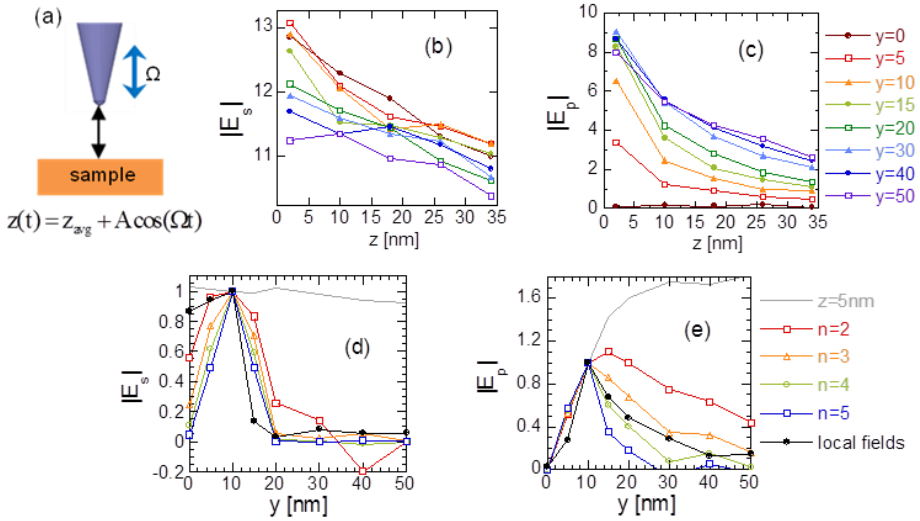

Fig. 5. (a) Model of the tip oscillation. Calculated far field signal magnitude (b) $|E_s|$ and (c) $|E_p|$ in arbitrary unit. Compare demodulated (d) s- and (e) p-polarization signals at higher harmonics (n = 2 ~5) with local profiles and signals without tip oscillation (fixed tip-sample distance of 5 nm). In plots (d) and (e), signals have been normalized to the number at y = 10 nm for each curve.

The demodulated signals at higher harmonics are shown in Figs. 5(d) and 5(e), together with the signal of constant tip height and the local field profiles. Signals at z = 5 nm without tip oscillation show a much slower spatial variation compared with the local spot size. With the consideration of tip oscillation and demodulation, the spot size approaches that of the local near field. At n = 3 - 5, the computed near field distribution are very close to those of the local profiles.

The calculated higher order signals can also be used to characterize the tip. The induced dipole-like radiation from the tip apex carries full information of local fields from the near-field into the far-field region via

$$\vec{E}_{scat} \propto \ddot{\alpha}\vec{E}_{local}, \qquad (2)$$

where $\ddot{\alpha}$ is a transfer matrix, also referred to as the effective polarizability tensor of the tip [1, 14, 30, 31]. It is geometry and material dependent, thus the magnitude and polarization state of the scattered light are strongly dependent on the tip. If the near field E_x is negligible, $\ddot{\alpha}$ is simplified as a 2 × 2 matrix with only the in-plane E_y and the out-of-plane E_z to be considered. For the bowtie aperture computed above, both local components are at the maximum at y = 10 nm with $E_y/E_z \approx 0.82$, while $E_s/E_p \approx 0.084$ for signals scattered by the Si tip at n = 3. Here we use fields at this location to compute $\ddot{\alpha}$. It has been shown that for a well-defined tip that is symmetric, as simulated here, the off-diagonal terms of $\ddot{\alpha}$ can be ignored [31]. The response of the Si tip is then characterized by $\alpha_{yy}/\alpha_{zz} \approx 0.102$. This also indicates that the tip interact much stronger with E_z than with E_y because the tip is vertically located [27].

#213948 - $15.00 USD Received 11 Jun 2014; revised 15 Jul 2014; accepted 18 Jul 2014; published 25 Jul 2014

Theoretically, the ratio should be independent of the position in the *xy* plane and the analysis can be done at a single location, provided that the profile of high harmonic signal represents the local field.

3. Experiments description

The experiment is carried out using a home-made transmission type s-NSOM system shown in Fig. 6, with a 633 nm HeNe laser as the excitation source. The system is based on a commercial AFM system CombiScope 1000 from AIST-NT, which also works in the reflection mode [32]. The laser beam is focused by a Nikon objective (NA = 0.3), which is mounted on a three-axis piezo scanner to provide accurate control of the focusing location. The AFM is operated in the tapping mode, with the probe oscillating at its fundamental resonance frequency. The scattered light is collected by a Mitutoyo objective (NA = 0.42) and directed to an avalanche photodiode detector (APD), which then outputs signal to a lock-in amplifier (HF2LI-MOD, Zurich Instruments) to perform demodulation. To avoid interfering with the measurements conducted in visible wavelength range, a 1300 nm diode laser is used for optical lever feedback in the AFM. The demodulated results are sent to the AFM controller for mapping purposes. Different polarizations of scattered light can be collected, chosen by a polarizer in front of the detector. Commercial Si AFM probe (ARROW-NCR, NanoWorld, 10~15 μm long) is used for all the measurements. The nominal radius of the tip apex is 10 nm and the scanning amplitude is set at 16 nm.

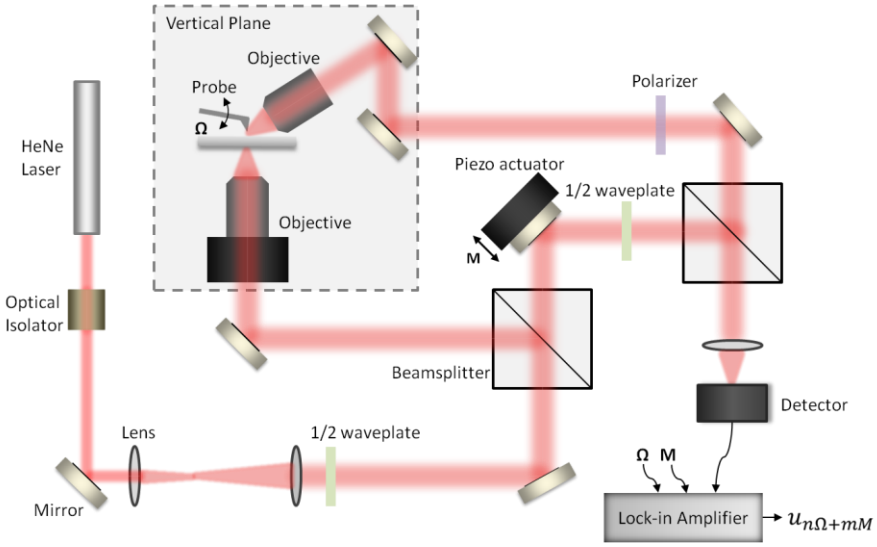

Fig. 6. Schematic of the transmission mode s-NSOM setup.

The sample is fabricated on a 60 nm thick gold film coated on a glass substrate. Bowtie apertures are milled using focused ion beam (FEI Nova 200 dual-beam FIB), and are designed to have an outline dimension of 250 nm with a 20 nm gap. However, as a result of FIB milling, the SEM images in Figs. 7(a) and 7(b) show a tapered cross section of the gap and an enlarged aperture size at the sample surface, respectively. In order to capture the side wall taper and the enlarged size, the numerical model of the sample is modified, with geometry parameters extracted from SEM images. In Fig. 7(c), the gap is ~20 nm at the glass/Au interface and ~80 nm at the Au/air interface (aperture exit). The outline dimension at the exit side in Fig. 7(d) is around 300 nm.

#213948 - $15.00 USD Received 11 Jun 2014; revised 15 Jul 2014; accepted 18 Jul 2014; published 25 Jul 2014

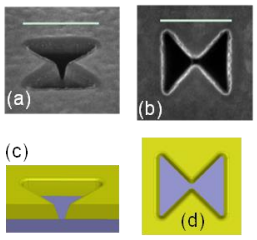

Fig. 7. (a, b) SEM images of the sample (scale bar: 300 nm), together with (c, d) models built in HFSS considering the real shape.

4. Discussion

Figure 8 shows the simulated near-field distributions for the actual aperture shape described in Fig. 7. The tapered gap degrades the field enhancement and localization. At a plane 8 nm above the aperture exit, the peak near-field enhancement factor is only 0.8 for E_z and 0.46 for E_y, compared with 2.34 and 2.52 if there is no side wall taper at the same height. The FWHM spot size for the local E_z is about 59 nm, as shown in Fig. 8(b). The near field interaction with tip becomes weaker as a result of the tapered gap, and only E_z can be mapped experimentally.

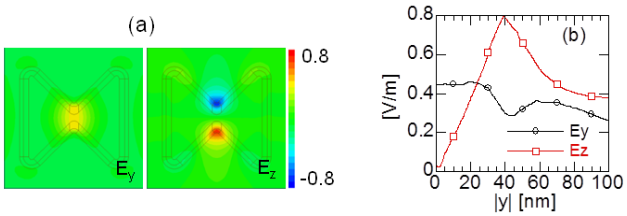

Fig. 8. (a) Near field distributions (400 × 400 nm^2) and (b) corresponding profiles.

Figure 9 shows the AFM topography image and optical images of $|E_p|$. We present here the results both with and without using the reference beam. The signals were detectable up to 5Ω when the interference beam was not used and up to 3Ω when the interference beam was used. As shown in Figs. 9(a) and 9(b), the two spots near the apexes of the aperture gap are consistent with the behavior of the local E_z. Significantly smaller spots at higher harmonics are observed and a comparison of the FWHM sizes is given in Fig. 9(c). Without using the reference beam, the spot size reduces from 300 nm at 1Ω to 62 nm at 5Ω, approaching that of the 59 nm local E_z spot evaluated at a plane 8 nm above the exit. It should be mentioned that the height 8 nm is chosen to better match the experimental data. In the actual experiment, it is likely that the scattered signal originates from a certain portion of the tip instead of a single point such as the apex of the tip. Similar approach has been used, for example, the near field 21 nm above the sample was used in [18] to compare with the measured data.

With the use of the reference beam, the spot size is further reduced compared with that without using the reference beam at the same harmonic order. In the non-interferometric measurements, there are asymetric tails especially at low harmonics, as can be observed in Fig. 9(a). This could be caused by the relative position of the probe and the side-mounted collection objective, resulting in more strongly modulated background scattering for the left part than the right part of the images. Figure 9(b) indicates that using the reference beam helps to minimize this asymmetry. The phase information is only obtained with the use of reference beam. Figures 9(d) and 9(e) show the line scans of the demodulated amplitude $|E_p|$ and phase φ_p, and the phase data is consistent with the expected local field from a bowtie aperture. Overall, Fig. 9 experimentally demonstrates that demodulation at higher harmonics helps to suppress background signals and obtain the images closer to the local field.

#213948 - $15.00 USD Received 11 Jun 2014; revised 15 Jul 2014; accepted 18 Jul 2014; published 25 Jul 2014

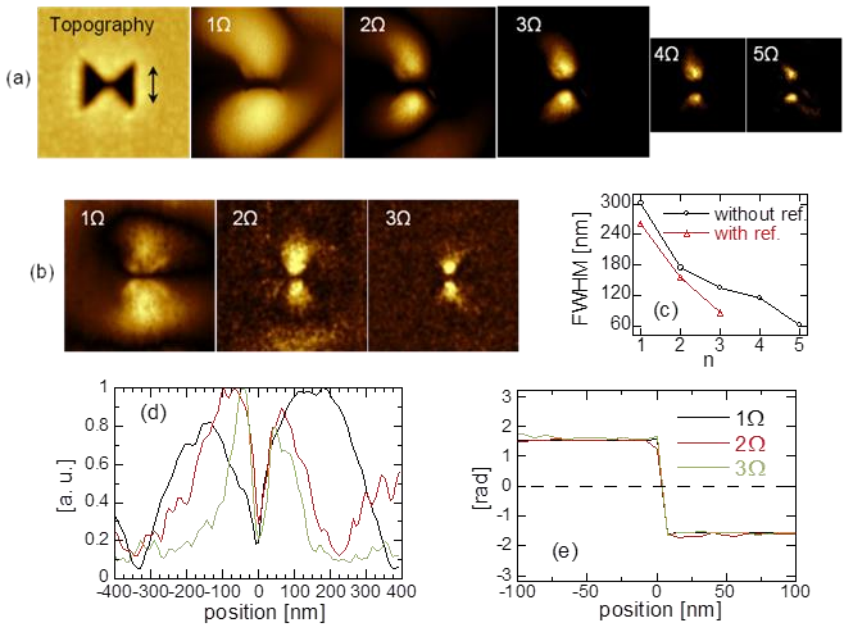

Fig. 9. AFM topography image and optical images of $|E_p|$ at different harmonic orders (a) without and (b) with the reference beam. The scan size is 0.8 × 0.8 μm^2 for the topography image and 1Ω to 3Ω, and 0.5 × 0.5 μm^2 for 4Ω and 5Ω. The black arrow in (a) indicates the incident polarization. (c) FWHM spot sizes as a function of the harmonic order, both with and without the reference beam. Line scans of the demodulated (d) amplitude and (e) phase in the presence of the reference beam.

5. Conclusion

In this work, numerical simulations are carried out to compute the interaction between an oscillating tip and the local near field produced by a nanostructure, and to compute high harmonic signals via a demodulation process. Dielectric tips such as a Si tip are found to be more appropriate for characterizing near fields. With a polarization-resolved collection of signals, it is possible to estimate the responses of the tip to different near field components, which helps to characterize the scattering of the tip. An important finding is that, with the increasing harmonic order, the simulated/measured spot size reduces, and is in closer agreement with the actual near field. Therefore, it is important to carry out s-NSOM measurements at higher order harmonics in order to obtain measurement results close to the actual near field.

Acknowledgments

Supports to this work by the Defense Advanced Research Projects Agency (Grant No. N66001-08-1-2037), the National Science Foundation (Grant No. CMMI-1120577), and ASTC- the Advanced Storage Technology Consortium are gratefully acknowledged.